Science for Energy and Environment
https://www.sciltp.com/journals/see

Article

Mechanism and Condition Optimization of Acid Leaching Recovery of $FePO_4$ from Iron–Phosphorus Slag after Lithium Extraction from $LiFePO_4$

Shanshan Luo [1,†], Yanyun Li [1,†], Qingyou Liu [2], Min Chen [1], Haitao Li [1], Xueli Chen [1], Haoyu Tan [1], Ting Yu [1], Liping Ai [1], Man Li [1] and Kai Zheng [1,*]

[1] School of Geography and Environmental Engineering, Gannan Normal University, Ganzhou 341000, China
[2] School of Materials and Environmental Engineering, Shenzhen Polytechnic University, Shenzhen 518055, China
* Correspondence: zhengkai@gnnu.edu.cn
† These authors contributed equally to this work.

How To Cite: Luo, S.; Li, Y.; Liu, Q.; et al. Mechanism and Condition Optimization of Acid Leaching Recovery of FePO4 from Iron–Phosphorus Slag after Lithium Extraction from $LiFePO_4$. *Science for Energy and Environment* **2026**, *3*(2), 11. https://doi.org/10.53941/see.2026.100011

Received: 5 August 2026
Revised: 16 September 2026
Accepted: 10 October 2026
Published: 16 October 2026

Abstract: The rapid expansion of lithium iron phosphate ($LiFePO_4$) applications has led to a surge in battery decommissioning, making comprehensive recovery of all components from spent $LiFePO_4$ batteries critical to the advancement of the industry. In this study, iron–phosphorus slag remaining after lithium extraction was recovered through washing, acid leaching, and precipitation. The resulting iron phosphate was characterized by SEM, EDS, and XRD to analyze its crystal structure, morphology, and chemical composition. Under optimized conditions, hydrochloric acid concentration of 7 mol/L, temperature of 70 °C, liquid-to-solid ratio of 15 mL/g, and leaching time of 5 h, the leaching rates of Fe and P exceeded 80%, with corresponding activation energies of 93.62 kJ/mol and 85.40 kJ/mol, respectively. Precipitation yielded iron phosphate with good crystallinity. Recycled and commercial-grade iron phosphate were each converted into lithium iron phosphate via carbothermal reduction and assembled into batteries for performance evaluation. The results demonstrated that precise control of the microstructure and morphology of the recycled material is essential for improving its electrochemical performance. This study provides guidance for the wet-process recovery of iron–phosphorus and $LiFePO_4$ from solid waste residues.

Keywords: battery recycling; iron phosphorus slag; iron phosphate; acid leaching; regeneration

1. Introduction

Compared with other power batteries, lithium-ion batteries offer clear advantages, including high energy density, fast charge-discharge capability, and long service life [1–4]. They have become the primary power source for electric vehicles, hybrid electric vehicles, and plug-in hybrids [5,6]. Among various cathode materials, lithium iron phosphate ($LiFePO_4$) exhibits excellent safety, long cycle life, good high-temperature performance, and environmental compatibility [7–10]. Its widespread industrial adoption is largely driven by environmental considerations [11–13].

In 2021, China produced 219.7 GWh of power batteries, of which 125.4 GWh were lithium iron phosphate batteries—surpassing ternary lithium batteries and accounting for 57.1% of total production, with a year-on-year increase of 263%. The installed capacity of lithium iron phosphate batteries has exceeded that of ternary batteries due to advantages in cost, safety, cycle life, environmental compatibility,

Copyright: © 2026 by the authors. This is an open access article under the terms and conditions of the Creative Commons Attribution (CC BY) license (https://creativecommons.org/licenses/by/4.0/).
Publisher's Note: Scilight stays neutral with regard to jurisdictional claims in published maps and institutional affiliations.

and technological maturity [14–17]. With the increasing use of lithium iron phosphate batteries in new energy vehicles, a significant volume of batteries is expected to reach end-of-life status in the near future. By 2030, the total retired capacity is projected to reach 177.85 GWh [18,19]. In this context, achieving comprehensive recovery of all components from spent $LiFePO_4$ batteries has become an important issue in resource recycling and environmental protection. Recent studies have emphasized that sustainable lithium extraction, battery recycling, and environmental protection should be advanced synergistically, and that comprehensive recovery of $FePO_4$ from spent $LiFePO_4$ is of great significance [20,21]. Current recycling processes primarily focus on recovering lithium, while iron and phosphorus are often discarded. The low recovery rate, harsh reaction conditions, and reliance on large volumes of acid–base reagents contribute to secondary pollution [22]. These processes generate substantial solid waste, including iron-phosphorus slag, black slag, and impurity-removal slag [23]. Most lithium recovery operations use wet selective extraction, but the resulting waste residues, if untreated, not only waste resources but also pose environmental hazards. Complete recovery of residual slag is necessary to prevent contamination and mitigate health risks [24].

Recycling methods for waste lithium iron phosphate batteries are primarily categorized into solid-phase and liquid-phase processes [25–28], with the latter being more widely adopted. Song et al. [29] synthesized nanosheet $FePO_4{\cdot}2H_2O$ through hydrothermal recrystallization and studied the effects of hydrochloric acid concentration on purity, particle size, crystal structure, and micromorphology. The addition of hydrochloric acid significantly improved the purity of iron phosphate in the phosphating slag. Tu et al. [30] developed a new method for recovering phosphorus and iron from lithium extraction slag (LES) by leaching and precipitation. $FePO_4{\cdot}2H_2O$ was obtained by adjusting the temperature and pH, and subsequently used to regenerate lithium iron phosphate cathode material, achieving a discharge capacity of 147 $mAh{\cdot}g^{-1}$ at 0.1 C and good cycling stability at 1 C. Huang et al. [31] synthesized $FePO_4{\cdot}2H_2O$ with 99.97% purity from $LiFePO_4$ waste via chemical co-precipitation. Bian et al. [32] employed phosphoric acid (H_3PO_4) for acid leaching of $LiFePO_4$ cathode waste to extract iron phosphate. The resulting nano-flower precursor $FePO_4{\cdot}2H_2O$, combined with Li_2CO_3 (as a lithium source) and glucose (as a carbon source and reducing agent), was calcined under a nitrogen atmosphere to prepare a new $LiFePO_4$/C composite by carbothermal reduction.

This study addresses the underutilization of iron and phosphorus resources discarded after lithium extraction from $LiFePO_4$ battery waste. Iron phosphate products were recovered from iron-phosphorus slag through washing, acid leaching, and precipitation. The process conditions for acid leaching were optimized, and the effects of acid concentration, temperature, leaching time, and liquid-to-solid ratio on leaching efficiency were investigated. This work proposes a complete recovery route for iron and phosphorus from $LiFePO_4$ waste, offering a viable solution for industrial waste reduction, environmental protection, and sustainable resource utilization.

2. Materials and Methods

2.1. Materials and Reagents

The lithium iron phosphate waste used in this study was sourced from a new energy enterprise in Jiangxi Province. The material comprises high-graphite battery waste residue referred to as iron-phosphorus slag obtained after lithium extraction from lithium iron phosphate cathode material, mixed with anode components. The elemental and phase compositions of the iron-phosphorus slag are presented in Table S1 and Figure S1. The primary elemental contents were as follows: iron (16%), phosphorus (9.04%), aluminum (1.05%), and copper (0.44%), along with various trace elements. The predominant phases included iron phosphate and graphite. The reagents employed in this study were hydrochloric acid (HCl, CP, 36.0–38.0%), ammonium dihydrogen phosphate ($NH_4H_2PO_4$, AR, ≥99.5%), anhydrous ethanol (C_2H_5OH, AR, ≥99.7%), sodium bicarbonate ($NaHCO_3$, ACS, 99%). All chemicals were purchased through a laboratory procurement platform.

2.2. Experimental Procedures

First, the iron-phosphorus slag was dried and pulverized using a high-speed crusher (FW10). The resulting powder was sieved to pass through a 200-mesh screen. The powder was stirred in deionized water for 1 h at a controlled liquid-to-solid ratio to remove the surface graphite layer. The material was then filtered, dried, and ground to uniformity. The experimental procedure is illustrated in Figure 1.

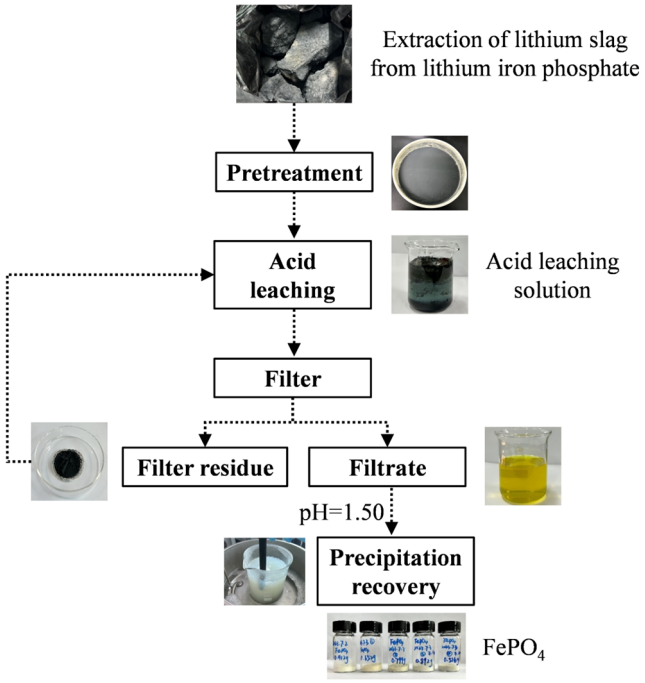


Figure 1. Flow of the experimental procedure.

Subsequently, iron and phosphorus were extracted from the residue using acid leaching. A defined mass of the ground residue was weighed using an analytical balance (ME403Te/02) and subjected to dissolution in hydrochloric acid under varied experimental conditions. The effects of four parameters on leaching performance were investigated, namely hydrochloric acid concentration (2, 3, 4, 5, 6, 7 mol/L), leaching temperature (30, 40, 50, 60, 70, 80 °C), liquid-to-solid ratio (10, 15, 20, 25 mL/g), and leaching time (2, 3, 4, 5 h). The acid leaching process dissolves major ions from the iron-phosphorus slag based on the reactions:

$$FePO_4 + 3HCl = FeCl_3 + H_3PO_4 \quad (1)$$

$$AlPO_4 + 3HCl = AlCl_3 + H_3PO_4 \quad (2)$$

The leaching efficiencies of iron and phosphorus were calculated using the following equations:

$$w = \frac{C_{1(Fe)}+C_{2(Fe)}}{C_{3(Fe)}} \times 100\% \quad (3)$$

The phosphorus leaching rate was calculated as follows:

$$w = \frac{C_{1(P)}+C_{2(P)}}{C_{3(P)}} \times 100\% \quad (4)$$

where C_1(Fe) and C_1(P) are the concentrations of Fe and P in the filtrate after pH adjustment (mg/L); C_2(Fe) and C_2(P) are the concentrations of Fe and P in the product (mg/L); and C_3(Fe) and C_3(P) are the concentrations of Fe and P in the raw material (mg/L). In the above calculations, C_1, C_2 and C_3 were normalized to unit mass of raw material. Specifically, the absolute masses of Fe and P in the leachate were obtained by multiplying their concentrations by the solution volume; the absolute masses of Fe and P in the product were obtained by multiplying the product mass by its elemental content; and the absolute masses of Fe and P in the raw material were obtained by multiplying the raw material mass by its elemental content. The mass balance errors for Fe and P were controlled within ±5%.

The iron phosphate was recovered by precipitation. The leachate obtained after acid leaching was maintained at 85 °C using a constant-temperature magnetic stirrer (DF101Se), and the pH was adjusted using a pH meter (FE28). Before pH adjustment, the molar ratio of iron to phosphorus was modified using ammonium dihydrogen phosphate and ferric chloride. Sodium bicarbonate ($NaHCO_3$) was then used to adjust the pH. The effects of Fe:P molar ratios (2:1, 1.5:1, 1:1, 1:1.5, and 1:2) and pH values (1.50, 1.60, 1.80, and 2.00) on the purity of iron phosphate were investigated. After the Fe:P ratio and pH were adjusted, the solution was aged at 85 °C for 3 h, followed by vacuum filtration for 3 h. The solid was washed with water and ethanol (3–5

times each), then dried at 105 °C for 2 h to obtain ferric phosphate dihydrate. The dihydrate was calcined at 300 °C for 2 h and then at 500 °C for another 2 h to yield anhydrous ferric phosphate.

Recovery of iron and phosphorus was calculated using the following equations:

$$w = \frac{C_{2(Fe)}}{C_{1(Fe)} + C_{2(Fe)}} \times 100\% \quad (5)$$

$$w = \frac{C_{2(P)}}{C_{1(P)} + C_{2(P)}} \times 100\% \quad (6)$$

2.3. Analytical Method

The content of metallic impurities in the iron phosphate products was analyzed using inductively coupled plasma mass spectrometry (ICP-MS, PE-NexION 1000, PerkinElmer, Shelton, CT, USA). Morphology and elemental composition were examined using scanning electron microscopy equipped with energy-dispersive X-ray spectroscopy (SEM-EDS, JSM-6460LV, JEOL, Tokyo, Japan). Iron content was determined by potassium dichromate titration [33–35]. Phosphorus content was measured by the gravimetric precipitation method. Elemental distribution and surface defects were characterized using Raman spectroscopy (InVia Reflex, Renishaw, Gloucestershire, UK). Crystalline phases were identified by X-ray diffraction (XRD) using a Bruker D8 Advance instrument (Bruker AXS GmbH, Karlsruhe, Germany) with a Cu Kα radiation source (λ = 0.15405 nm).

3. Results and Discussion

3.1. Optimization of Dissolution Conditions

The effects of hydrochloric acid concentration, leaching temperature, liquid–solid ratio, and leaching time on the leaching rates of iron and phosphorus were investigated through single-factor experiments. The leaching performance under various conditions is shown in Figure 2.

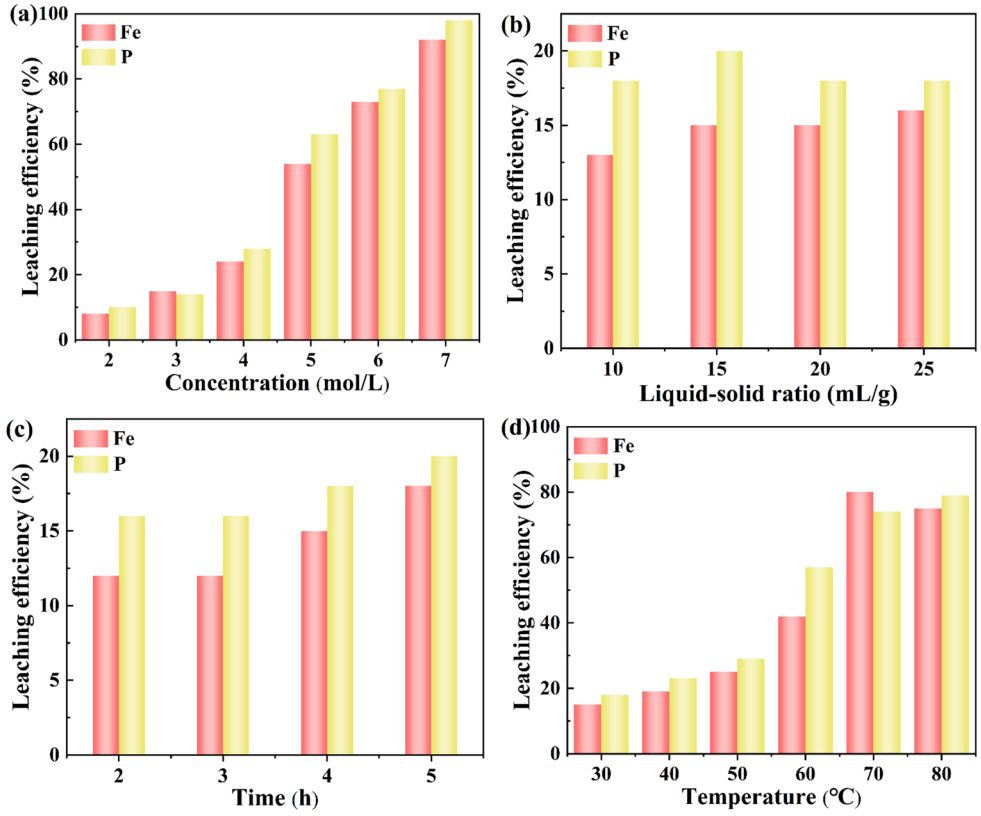


Figure 2. (**a**) Effect of hydrochloric acid concentration on the leaching rates of iron and phosphorus (conditions: temperature = 30 °C, liquid–solid ratio = 15 mL/g, time = 4 h); (**b**) Effect of liquid–solid ratio (conditions: concentration = 3 mol/L, temperature = 30 °C, time = 4 h); (**c**) Effect of time (conditions: concentration = 3 mol/L, temperature = 30 °C, liquid–solid ratio = 15 mL/g); (**d**) Effect of temperature (conditions: concentration = 3 mol/L, liquid–solid ratio = 15 mL/g, time = 4 h).

3.1.1. Effect of Hydrochloric Acid Concentration

Leaching was conducted for 4 h at 30 °C using hydrochloric acid solutions of varying concentrations (2–7 mol/L) with a fixed liquid–solid ratio of 15 mL/g. The effect of acid concentration on the leaching rates of iron and phosphorus was examined. Increasing the acid concentration generally enhanced the reaction intensity, improving the dissolution rate. As shown in Figure 2a, the leaching rates of Fe and P increased continuously with increasing HCl concentration and reached a maximum at 7 mol/L. Since concentrations above 7 mol/L were not tested in this study, 7 mol/L is not claimed as the absolute optimum, but rather as the condition giving the highest leaching efficiency within the investigated range. Further increasing the acid concentration might improve leaching, but would significantly increase acid volatilization losses, operational risks, and the amount of alkali required for subsequent neutralization. Therefore, 7 mol/L was selected for subsequent experiments.

3.1.2. Effect of Liquid-Solid Ratio

The acid concentration and temperature were fixed at 3 mol/L and 30 °C, respectively, and leaching was performed for 4 h. Liquid–solid ratios of 10, 15, 20, and 25 mL/g were tested to determine their effect on the leaching efficiency. As shown in Figure 2b, the leaching rates of iron and phosphorus initially increased with the liquid–solid ratio but later decreased. This trend was attributed to the high graphite content in the raw materials, which limited further leaching at higher ratios. A ratio of 15 mL/g resulted in the highest phosphorus leaching rate, while the iron leaching rate remained relatively stable. Moreover, using 15 mL/g minimized acid consumption and, consequently, reduced the amount of sodium bicarbonate required for pH adjustment. This minimized chemical usage and cost. Thus, 15 mL/g was selected as the optimal liquid–solid ratio.

3.1.3. Effect of Leaching Time

The hydrochloric acid concentration was fixed at 3 mol/L, the leaching temperature was maintained at 30 °C, and the liquid–solid ratio was set at 15 mL/g. The effect of leaching time (2, 3, 4, and 5 h) on the leaching rates of iron and phosphorus was investigated. Leaching time is a key parameter influencing extraction efficiency. In general, prolonged reaction time improves the leaching rate. Insufficient duration may lead to incomplete extraction of the target elements, while excessive leaching time can result in unnecessary solvent consumption and increased energy usage. As shown in Figure 2c, the leaching rates of both iron and phosphorus increased progressively with time. However, beyond a certain point, further increases in time yield diminishing returns relative to the added cost and energy input. Based on this tradeoff, 5 h was selected as the optimal leaching time for subsequent experiments.

3.1.4. Effect of Leaching Temperature

The effect of temperature was evaluated using a fixed acid concentration of 3 mol/L, a liquid–solid ratio of 15 mL/g, and a leaching time of 4 h. Experiments were conducted at temperatures of 30, 40, 50, 60, 70, and 80 °C. Increasing the temperature enhances the kinetic energy of molecules, accelerates their motion, and promotes diffusion, thereby improving the leaching rate. As shown in Figure 2d, both iron and phosphorus leaching rates increased with temperature. Up to 70 °C, the phosphorus leaching rate rose rapidly, and the iron leaching rate continued to increase. Beyond 70 °C, phosphorus leaching plateaued, while iron leaching declined. This decline may be attributed to the intensified thermal motion, which disrupts the directional transport of free electrons and reduces dissolution efficiency. Therefore, 70 °C was selected as the optimal leaching temperature.

3.2. Leaching Kinetics of Iron and Phosphorus Residue in Hydrochloric Acid

The primary component of the iron–phosphorus slag is iron phosphate. Based on prior studies [36,37], the shrinking core model is commonly applied to describe metal dissolution in cathode materials from spent lithium-ion batteries. In this model, the leaching reaction begins at the particle surface and progresses inward toward the core. Once the chemical reaction is complete, the products diffuse from the particle interior into the solution. Equations (7)–(9) represent the kinetic expressions for different rate-controlling steps [38].

$$kt = X \tag{7}$$

$$kt = 1 - 3(1 - X)^{2/3} + 2(1 - X) \quad (8)$$

$$kt = (1 - X)^{2/3} - 1 \quad (9)$$

where k, t, and X represent the kinetic constant, leaching time, and fractional leaching rate, respectively. Based on Table S2 and the comparison between curves a_1, b_1, c_1 and a_2, b_2, c_2 in Figure 3, the reaction rate constant increased with temperature. This trend reflects the endothermic nature of the leaching process, where higher temperatures accelerate the reaction rate. The leaching behavior of both iron and phosphorus aligned most closely with the in-layer diffusion model of the solid product. Among the three kinetic models, this model exhibited the best fit, with R^2 values exceeding 0.99 across all curves, indicating that the leaching process was primarily controlled by internal diffusion.

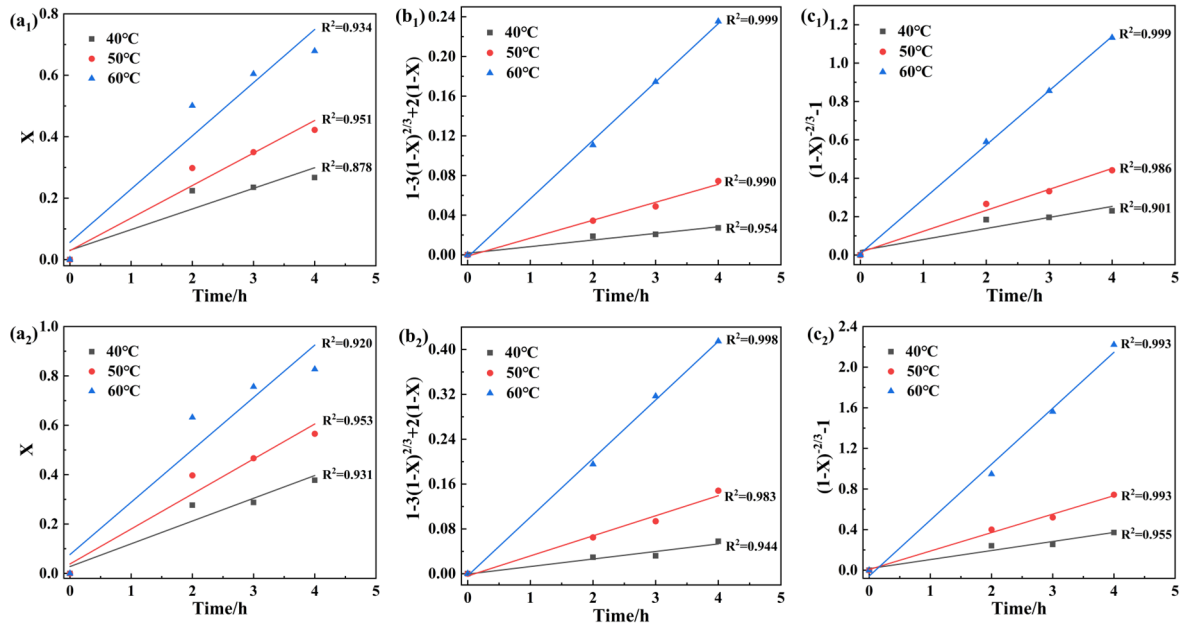


Figure 3. Leaching kinetics of iron and phosphorus from iron–phosphorus slag at various temperatures: (**a_1**) External diffusion (liquid boundary layer control, Fe). (**b_1**) Internal diffusion (solid product layer control, Fe). (**c_1**) Surface chemical reaction control (Fe). (**a_2**) External diffusion (liquid boundary layer control, P). (**b_2**) Internal diffusion (solid product layer control, P). (**c_2**) Surface chemical reaction control (P).

According to the Arrhenius equation, the apparent activation energy was determined by plotting ln k_b versus 1/T using data fitted to the internal diffusion model for both iron and phosphorus. The fitted curves are shown in Figure S2a,b. Based on the slopes, the apparent activation energies for the leaching of iron and phosphorus were calculated as 93.62 kJ/mol and 85.40 kJ/mol, respectively.

It should be noted that the apparent activation energies of Fe and P reached 93.62 kJ/mol and 85.40 kJ/mol, respectively. It is generally accepted that internal diffusion-controlled processes exhibit activation energies below ~20 kJ/mol, whereas surface chemical reaction-controlled processes usually show activation energies above ~40 kJ/mol. The relatively high activation energies obtained here suggest that the leaching process may not be controlled solely by internal diffusion, but rather by a mixed mechanism involving both internal diffusion and surface chemical reaction. Although the internal diffusion model gave $R^2 > 0.99$, the high activation energies indicate that the chemical dissolution step at the reaction interface still plays an important role. Therefore, simply attributing the process to internal diffusion control is not rigorous, and future work should further verify the mechanism using mixed-control models.

3.3. Orthogonal Experiment

An orthogonal experiment with four factors at four levels was designed to optimize the leaching conditions, building on the results of the single-factor experiments.

The factor levels are summarized in Table S3, and the experimental results are shown in Table S4. Range analysis indicated the following order of influence on the leaching rate of iron: Leaching

concentration > Liquid–solid ratio > Leaching temperature > Leaching time. For phosphorus, the influence ranked as follows: Liquid–solid ratio > Leaching concentration > Leaching time > Leaching temperature.

Based on these results, the optimal leaching conditions for iron and phosphorus were as follows: hydrochloric acid concentration of 7 mol/L, leaching temperature of 70 °C, liquid–solid ratio of 15 mL/g, and leaching time of 5 h. Under these conditions, the leaching efficiencies of Fe and P reach 83.38% and 96.35%, respectively.

3.4. Effects of Different Precipitation Conditions on Iron Phosphate Products

Single-factor experiments were conducted under the following conditions: sodium bicarbonate concentration of 0.5 mol/L, temperature of 85 °C, and aging time of 3 h. The effects of pH and Fe:P molar ratio on the recovery of iron and phosphorus from iron–phosphorus slag were evaluated to identify optimal precipitation conditions.

In this section, the precipitation experiments used a leachate obtained under the conditions of 6 mol/L HCl, 70 °C, liquid-to-solid ratio of 10 mL/g, and 4 h. The reasons are as follows: under these conditions, the leachate volume is moderate and the Fe and P concentrations are relatively high, which facilitates precise control of pH and Fe:P ratio and avoids reagent waste caused by a high liquid-to-solid ratio. It should be noted that these conditions differ from the optimal leaching conditions obtained by the orthogonal experiments in Section 3.3. This section focuses on the precipitation stage; therefore, a representative leachate was selected for precipitation experiments rather than repeating the optimal leaching conditions. Future work will verify the precipitation performance using leachate generated under the orthogonal optimized leaching conditions.

3.4.1. Effects of pH

A 10 g sample was leached under the following conditions: hydrochloric acid concentration of 6 mol/L, leaching temperature of 70 °C, liquid–solid ratio of 10, stirring, and a reaction time of 4 h. Four 20 mL aliquots of the leachate were adjusted to pH 1.50, 1.60, 1.80, and 2.00 to investigate the effect of pH on precipitation. As shown in Figure 4a, pH had minimal effect on the recovery rate, with both Fe and P recovery exceeding 95%. The acidic range (pH 1.50–2.00) allowed H^+ and $H_2PO_4^-$ to react with $NaHCO_3$, producing H_2O and PO_4^{3-}, while Fe^{3+} formed dihydrate iron phosphate ($FePO_4{\cdot}2H_2O$) with PO_4^{3-}. To minimize reagent cost, pH = 1.50 was selected as optimal. At pH > 2.5, $FePO_4$ may convert to $Fe(OH)_3$, releasing PO_4^{3-} and reducing phosphorus recovery. Therefore, higher pH values were excluded from analysis [39].

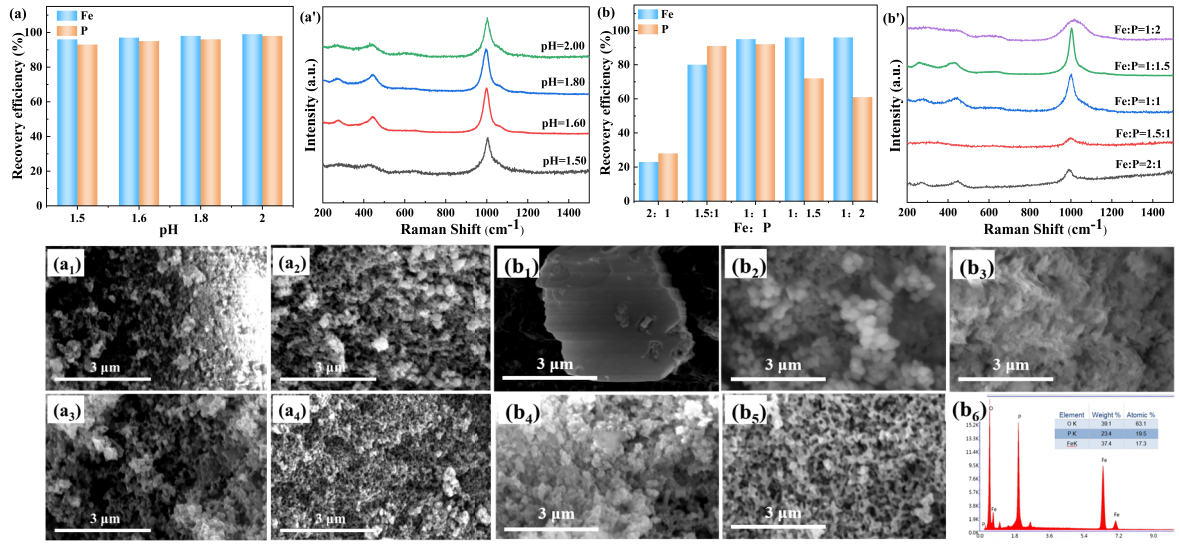


Figure 4. (**a**) Effect of pH on Fe and P recovery. (**a'**) Raman spectra of iron phosphate at different pH values. (**b**) Effect of Fe:P molar ratio on Fe and P recovery. (**b'**) Raman spectra of iron phosphate at various Fe:P ratios. SEM–EDS of iron phosphate: (a_1–a_4) pH = 1.50, (**b_1**) Fe:P = 2:1, (**b_2**) Fe:P = 1.5:1, (**b_3**) Fe:P = 1:1, (**b_4**) Fe:P = 1:1.5, and (**b_5**) Fe:P = 1:2.

3.4.2. Effect of Fe:P Molar Ratio

Under the same leaching conditions, the effect of Fe:P molar ratios (2:1, 1.5:1, 1:1, 1:1.5, 1:2) on iron phosphate formation was investigated. As shown in Figure 4b, Fe and P recovery rates exceeded 95% across all ratios. The highest recovery occurred at a molar ratio of 1:1, indicating that stoichiometric balance favored the complete precipitation of Fe^{3+} and PO_4^{3-} as dihydrate iron phosphate.

3.5. Sample Characterization and Analysis

3.5.1. Phase, Morphology, and Elemental Composition

Raman spectroscopy was conducted to characterize the iron phosphate product. As shown in Figure 4a',b', all spectra exhibited strong peaks near 1000 cm^{-1}. The characteristic stretching vibration peak of $FePO_4$ appears at 1009 cm^{-1} [40], with additional $FePO_4$ vibrations observed at 959 cm^{-1}, 948 cm^{-1}, and 1091 cm^{-1}. The symmetric stretching vibration of PO_4^{3-} (ν_1) occurs at 1026 cm^{-1}, and the asymmetric stretching (ν_2) appears near 949 cm^{-1} [41]. The observed spectral shifts suggest the presence of crystal water in the product, indicating the formation of hydrated iron phosphate. The spectrum at pH = 1.50 and Fe:P = 1:1 shows distinct peaks with minimal background noise, confirming these as the optimal conditions for high-purity product formation.

Scanning electron microscopy (SEM) was used to observe particle morphology. Figure 4a_1–a_4 show $FePO_4$ formed at pH values of 1.50, 1.60, 1.80, and 2.00, respectively. Increasing pH led to a gradual decrease in particle size, suggesting that nucleation dominated over crystal growth during synthesis.

Figure 4b_1–b_5 present SEM images of samples prepared at Fe:P molar ratios of 2:1, 1.5:1, 1:1, 1:1.5, and 1:2. The particles displayed layered structures with thicknesses of several hundred nanometers and size distributions ranging from 100 nm to 5 μm. Minor agglomeration was observed, contributing to D_{50} values exceeding 10 μm. As the Fe:P ratio decreased, particle size decreased, and morphology became increasingly irregular. This was attributed to the higher pH and increased free PO_4^{3-} concentration, which enhanced nucleation relative to growth. At a 1:1 ratio (Figure 4b_3), particles were uniformly dispersed with amorphous morphology, which is desirable for battery-grade lithium iron phosphate. The corresponding EDS analysis (Figure 4b_6) confirmed the presence of Fe and P, with a molar ratio of approximately 1:1 and minimal impurities, consistent with the stoichiometry of $FePO_4 \cdot 2H_2O$. XRD analysis was performed on the recovered product under optimal conditions. As shown in Figure 5, all diffraction peaks matched those of standard $FePO_4$ (PDF#77-0094). The product exhibited well-defined peaks, indicating high crystallinity. The results confirm that Fe was recovered as $FePO_4 \cdot 2H_2O$. Upon heat treatment and dehydration, a crystalline $FePO_4$ phase was obtained.

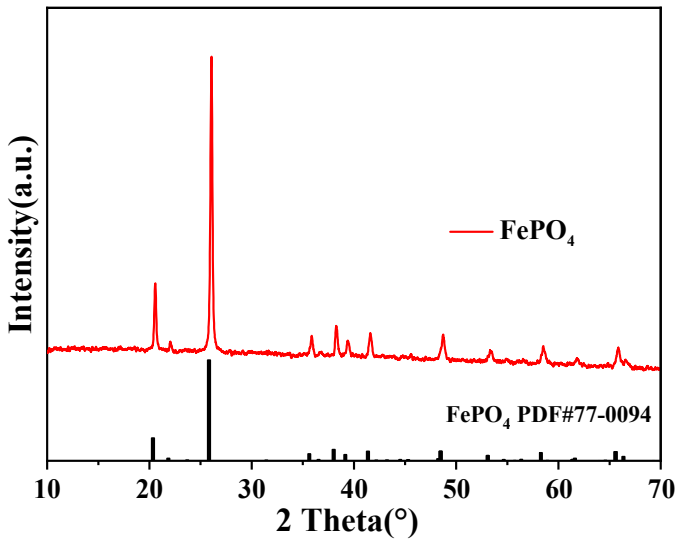


Figure 5. XRD pattern of iron phosphate sample.

3.5.2. Product Purity and Comparison with Battery-Grade Standards

The purified product was analyzed to determine its elemental composition. Iron content was measured by potassium dichromate titration, phosphorus content by precipitation method, and trace metals by ICP-

MS. The results are presented in Tables S5 and S6. The data confirm that the product composition meets the specifications for battery-grade iron phosphate, indicating its suitability for industrial recycling.

3.6. Recycled Lithium Iron Phosphate Cathode Material

Considering the volatility of lithium at elevated temperatures and its low intercalation efficiency into $FePO_4$, the effect of lithium supplementation on the synthesis of lithium iron phosphate ($LiFePO_4$) was investigated. The recovered $FePO_4$ was mixed with Li_2CO_3 (as a lithium source) and 10 wt% glucose (as a carbon source and reducing agent), adjusting the elemental molar ratio to Li:Fe:P = 1.03:1:1. The mixture was calcined at 300 °C for 2 h and then at 750 °C for 8 h under N_2 atmosphere to obtain the regenerated $LiFePO_4$ cathode material.

3.6.1. Morphology and Structure of Recycled Lithium Iron Phosphate Cathode Material

The synthesized lithium iron phosphate was characterized by XRD. As shown in Figure 6, samples prepared using water as the solvent exhibited additional impurity peaks, whereas those synthesized with ethanol showed diffraction patterns consistent with the standard $LiFePO_4$ reference (PDF#40-1499). The diffraction peaks were sharp and well-defined, with no evidence of excess carbon, confirming the successful formation of high-purity $LiFePO_4$.

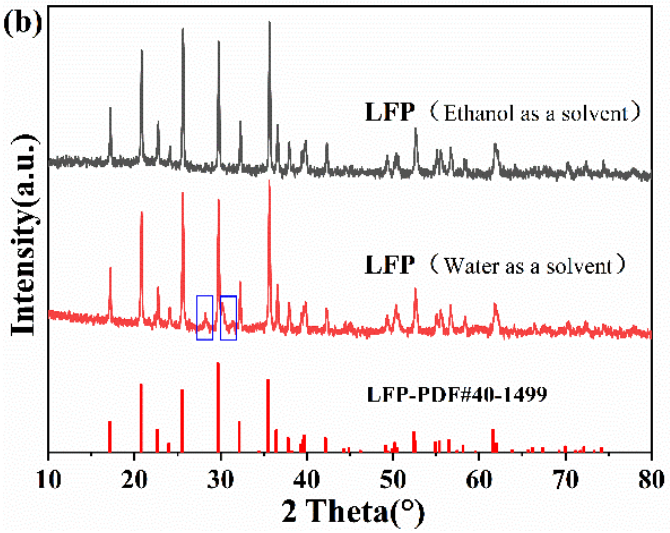


Figure 6. XRD pattern of lithium iron phosphate.

XPS analysis was conducted on both the $FePO_4$ precursor and the regenerated $LiFePO_4$. The elemental contents of C, O, P, and Fe in $FePO_4$ were 3.05%, 18.94%, 4.18%, and 2.14%, respectively. In the regenerated $LiFePO_4$, the corresponding contents were 12.39%, 10.80%, 2.09%, and 1.00%. The XPS full spectrum of $LiFePO_4$ (Figure S3) revealed characteristic orbitals of Fe 2p, O 1s, C 1s, and P 2p. As shown in Figure 7a–d, the C 1s spectra exhibited peaks near 284.8 eV and 289 eV, corresponding to C–C and C–O bonds, respectively. The O 1s spectrum confirmed the presence of P–O (531.59 eV) and C–O (532.87 eV) bonds. High-resolution P 2p spectra (Figure 7e,f) displayed characteristic peaks of P $2p_3/_2$ at approximately 133 eV and P $2p_1/_2$ at approximately 134 eV.

The binding energies and atomic concentrations of Fe 2p orbitals in $FePO_4$ and regenerated $LiFePO_4$ are listed in Table S8. As shown in Figure 8a,b, the high-resolution Fe 2p spectra consist of eight peaks corresponding to Fe $2p_3/_2$, Fe $2p_1/_2$, and their respective satellite peaks. In $FePO_4$ (Figure 8a), peaks at 711.66 eV and 723.44 eV are assigned to Fe^{2+} $2p_3/_2$ and Fe^{2+} $2p_1/_2$, respectively, while peaks at 712.96 eV and 726.61 eV correspond to Fe^{3+} $2p_3/_2$ and Fe^{3+} $2p_1/_2$. In regenerated $LiFePO_4$ (Figure 8b), peaks at 708.99 eV and 722.19 eV are attributed to Fe^{2+}, and those at 710.83 eV and 723.83 eV to Fe^{3+}. The Fe 2p spectrum of $FePO_4$ shows a higher atomic ratio of Fe^{3+} relative to Fe^{2+}. In contrast, regenerated $LiFePO_4$ exhibits a higher Fe^{2+} content than Fe^{3+}, indicating effective reduction of Fe^{3+} to Fe^{2+} during regeneration. These results confirm the successful restoration of the desired Fe^{2+} oxidation state in $LiFePO_4$.

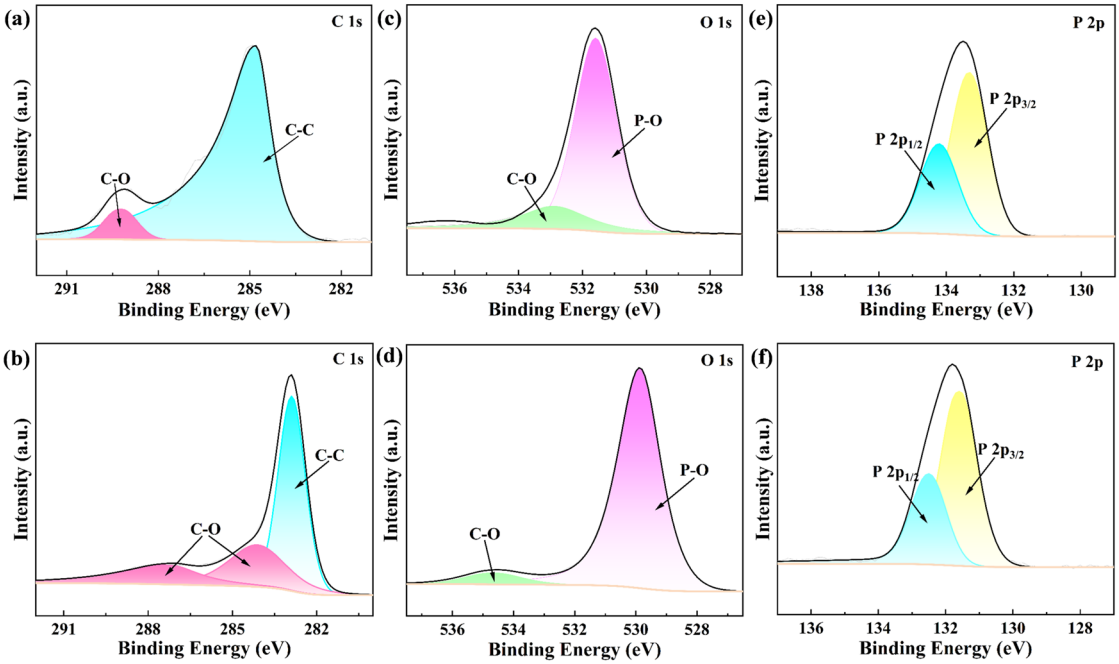


Figure 7. XPS spectra of $FePO_4$ (**a**: C 1s, **c**: O 1s, **e**: P 2p) and $LiFePO_4$ (**b**: C 1s, **d**: O 1s, **f**: P 2p).

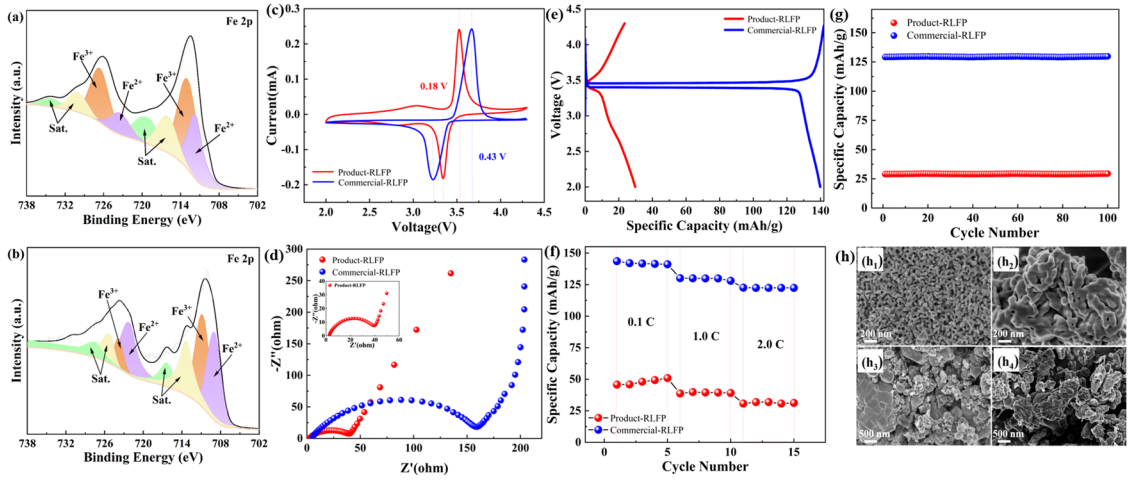


Figure 8. XPS spectra of (**a**) $FePO_4$ (Fe 2p) and (**b**) regenerated Li $FePO_4$ (Fe 2p); (**c**) CV curve of regenerated $LiFePO_4$; (**d**) EIS spectrum; (**e**) charge–discharge curve; (**f**) rate performance at different current rates; (**g**) cycle performance at 1C; (**h_1**) SEM of recovered $FePO_4$; (**h_2**) SEM of commercial $FePO_4$; (**h_3**) SEM of regenerated $LiFePO_4$ from recovered $FePO_4$; (**h_4**) SEM of regenerated $LiFePO_4$ from commercial $FePO_4$.

3.6.2. Electrochemical Performance

Lithium iron phosphate cathode materials were synthesized from both recovered and commercial iron phosphate through the carbothermal reduction method. These materials were assembled into coin cells for electrochemical testing. The cyclic voltammetry (CV) curve of regenerated $LiFePO_4$ is shown in Figure 8c. In both samples, the redox peaks correspond to the Fe^{3+}/Fe^{2+} redox couple. The small potential gap between oxidation and reduction peaks indicates low electrode polarization and smooth Li^+ intercalation. The electrochemical impedance spectroscopy (EIS) results (Figure 8d) show charge transfer resistances (R_{ct}) of approximately 48 Ω for regenerated $LiFePO_4$ and 155 Ω for commercial $LiFePO_4$. Both values indicate favorable electrochemical reactivity. The charge–discharge profiles at 0.1 C are presented in Figure 8e. The specific capacity of $LiFePO_4$ synthesized from commercial $FePO_4$ reached approximately 140 mAh/g, while the material derived from recycled $FePO_4$ exhibited a reduced capacity of ~48 mAh/g. Rate performance at varying current densities is shown in Figure 8f. At 0.1, 1, and 2 C, the discharge capacities of $LiFePO_4$ from commercial sources were approximately 140, 130, and 122.5 mAh/g, respectively. In contrast, $LiFePO_4$ from recycled $FePO_4$ delivered capacities of 48, 37, and 30 mAh/g. Cycling performance at 1 C is shown in Figure

8g. The capacity of $LiFePO_4$ from commercial $FePO_4$ remained stable at ~130 mAh/g, while the recycled counterpart retained only ~30 mAh/g. These results demonstrate that the synthesis method is technically feasible. However, the electrochemical performance of Li $FePO_4$ from recovered $FePO_4$ remains suboptimal. The likely cause is contamination from residual graphite impurities, which are difficult to fully remove due to the combined treatment of cathode and anode materials during lithium extraction. These residuals may go undetected post-leaching but still affect performance. Additionally, poor control of carbothermal reduction conditions may result in structural defects such as irregular morphology and oversized particles in the regenerated cathode material.

SEM was used to compare the morphology and microstructure of recycled and commercial iron phosphate. As shown in Figure 8h_1,h_2, the recycled iron phosphate exhibited a reticular structure with uniformly distributed fine particles. By contrast, the commercial iron phosphate showed a clustered morphology, which enhances lithium-ion diffusion and intercalation. $LiFePO_4$ cathode materials were then regenerated using both types of precursors, and their structural features were compared, as shown in Figure 8h_3,h_4. The $LiFePO_4$ derived from recycled iron phosphate displayed irregular spherical or block-like particles of non-uniform size, with clear evidence of particle sintering. The sintering of primary particles led to the formation of larger secondary aggregates. Conversely, the $LiFePO_4$ synthesized from commercial iron phosphate consisted of uniformly distributed fine particles with a narrow size distribution. The finer and more homogeneous structure of $LiFePO_4$ from commercial precursors promotes lithium-ion transport by facilitating diffusion pathways within the solid medium. The inferior electrochemical performance of the recycled sample is primarily attributed to its irregular morphology and larger particle size. Another contributing factor is the use of recycled iron-phosphorus slag sourced from industrial processes as the raw material, consisting of mixed cathode and anode waste. Despite acid leaching and purification, trace amounts of residual graphite may persist undetected, negatively affecting the microstructure and electrochemical properties. These findings highlight the importance of precise control over the microstructure during the recycling and regeneration process to enhance the performance of the resulting cathode materials.

4. Conclusions

This paper proposed a method for recovering iron and phosphorus from solid waste iron–phosphorus slag through washing, acid leaching, precipitation, and thermal reduction. Optimal leaching and precipitation conditions were determined through single-factor and orthogonal experiments, and the leaching kinetics were investigated. The resulting iron phosphate exhibited a complete crystal structure, uniform distribution, and small particle size. $LiFePO_4$/C was regenerated from $FePO_4$, Li_2CO_3, and glucose through a carbothermal reduction approach. $LiFePO_4$ regenerated from commercial iron phosphate and that derived from commercial iron phosphate were compared. The structural morphology of the regenerated $LiFePO_4$was assessed through XRD and SEM, and the electrochemical properties were assessed through battery performance testing. The results confirmed the feasibility of the regeneration method. However, the specific capacity of the $LiFePO_4$ cathode prepared from recycled iron phosphate reached only approximately 30 mAh/g at a current density of 1 C, indicating limited performance. These findings highlight challenges associated with the regeneration process. Effective recycling requires not only improved separation of cathode and anode materials but also precise control over the microstructure of the regenerated $LiFePO_4$ to ensure favorable electrochemical characteristics. This work offers a reference for the wet-process recovery of iron–phosphorus slag and the subsequent preparation of lithium iron phosphate.

From an engineering perspective, the proposed process uses hydrochloric acid as the leaching agent and sodium bicarbonate as the precipitant, operates under mild conditions (70–80 °C, ambient pressure), avoids organic solvents, and relies on readily available and low-cost reagents. The leachate can be recycled for subsequent batches, indicating good potential for industrial scale-up. NaCl in the precipitation mother liquor can be recovered by evaporation crystallization, reducing wastewater discharge. Future work should focus on optimizing the pre-separation of cathode and anode materials, minimizing the influence of residual graphite on product purity, and controlling nucleation and growth to tailor the particle size and morphology of the $FePO_4$ precursor, thereby improving the electrochemical performance of regenerated $LiFePO_4$.

Supplementary Materials

The following supporting information can be downloaded at: https://media.sciltp.com/articles/others/2610141704325664/SEE-26080034-SI.pdf, Figure S1: XRD pattern of iron-phosphorus slag; Figure S2.

(a) and (b) are the fitting curves of $\ln k_b$-1/T in the leaching process of iron and phosphorus, respectively; Figure S3. XPS full spectrum of iron phosphate and lithium iron phosphate; Table S1: Composition of lithium iron phosphate waste (mass fraction); Table S2. The fitted rate constants of iron and phosphorus leaching at different temperatures and their correlation coefficients; Table S3. Level table of orthogonal experimental factors; Table S4. Orthogonal experimental data and results; Table S5. Iron and phosphorus contents of iron phosphate; Table S6. Quality index of iron phosphate (w/%); Table S7. The content of C, O, P and Fe elements in iron phosphate and lithium iron phosphate; Table S8. Fe 2p orbitals of iron phosphate and lithium iron phosphate.

Author Contributions

S.L.: conceptualization, methodology, investigation, writing—original draft; Y.L.: conceptualization, methodology, validation, writing—original draft; Q.L.: data curation, formal analysis; M.C.: investigation, visualization; H.L.: investigation, resources; X.C.: data curation, validation; H.T.: methodology; T.Y.: investigation, validation; L.A.: resources, data curation; M.L.: visualization; K.Z.: conceptualization, supervision, funding acquisition, writing—review and editing, project administration.

Funding

This work was financially supported by the National Natural Science Foundation of China (40367055), the Science and Technology Research Project of Jiangxi Provincial Department of Education (GJJ 211425), the Open Research Fund Program of Jiangxi Key Laboratory of Low-Carbon Solid Waste Recycling (Gannan Normal University No.20212 BCD 42015).

Data Availability Statement

The authors confirm that the data supporting the findings of this study are available within the article.

Conflicts of Interest

The authors declare no conflict of interest.

Use of AI and AI-Assisted Technologies

No AI tools were utilized for this paper.

References

1. Chen, X.D.; Yang, H.Y.; Wun, J.S.; et al. Life prediction of lithium-ion battery based on a hybrid model. *Energy Explor. Exploit.* **2020**, *38*, 1854–1878. https://doi.org/10.1177/0144598720911724.
2. Xu, B.; Oudalov, A.; Ulbig, A.; et al. Modeling of Lithium-Ion Battery Degradation for Cell Life Assessment. *IEEE Trans. Smart Grid* **2018**, *9*, 1131–1140. https://doi.org/10.1109/tsg.2016.2578950.
3. Li, X.; Qiao, Y.; Guo, S.; et al. A New Type of Li-Rich Rock-Salt Oxide $Li_2Ni_{1/3}Ru_{2/3}O_3$ with Reversible Anionic Redox Chemistry. *Adv. Mater.* **2019**, *31*, 1807825. https://doi.org/10.1002/adma.201807825.
4. Zhao, J.; Qu, J.; Qu, X.; et al. Cathode electrolysis for the comprehensive recycling of spent lithium-ion batteries. *Green Chem.* **2022**, *24*, 6179–6188. https://doi.org/10.1039/d2gc02118h.
5. Zhang, X.; Li, Z.; Luo, L.; et al. A review on thermal management of lithium-ion batteries for electric vehicles. *Energy* **2022**, *238*, 121652. https://doi.org/10.1016/j.energy.2021.121652.
6. Ralls, A.M.; Leong, K.; Clayton, J.; et al. The Role of Lithium-Ion Batteries in the Growing Trend of Electric Vehicles. *Materials* **2023**, *16*, 6063. https://doi.org/10.3390/ma16176063.
7. Wang, Y.H.; Wu, J.J.; Hu, G.C.; et al. Recovery of Li and Fe from spent lithium iron phosphate using organic acid leaching system. *Trans. Nonferrous Met. Soc. China* **2024**, *34*, 336–346. https://doi.org/10.1016/s1003-6326(23)66402-7.
8. Song, Y.; Xie, B.; Song, S.; et al. Regeneration of $LiFePO_4$ from spent lithium-ion batteries via a facile process featuring acid leaching and hydrothermal synthesis. *Green Chem.* **2021**, *23*, 3963–3971. https://doi.org/10.1039/d1gc00483b.
9. Tang, D.; Ji, G.; Wang, J.; et al. A Multifunctional Amino Acid Enables Direct Recycling of Spent $LiFePO_4$ Cathode Material. *Adv. Mater.* **2024**, *36*, 2309722. https://doi.org/10.1002/adma.202309722.
10. Chen, B.; Liu, M.; Cao, S.; et al. Direct regeneration and performance of spent $LiFePO_4$ via a green efficient hydrothermal technique. *J. Alloys Compd.* **2022**, *924*, 166487. https://doi.org/10.1016/j.jallcom.2022.166487.

11. Tian, X.; Ma, Q.; Xie, J.; et al. Environmental impact and economic assessment of recycling lithium iron phosphate battery cathodes: Comparison of major processes in China. *Resour. Conserv. Recycl.* **2024**, *203*, 107449. https://doi.org/10.1016/j.resconrec.2024.107449.
12. Kyaw, A.M.M.; Panomsuwan, G.; Munprom, R. Solid-State Reaction Synthesis and Characterization of Mn-Doped $LiFePO_4$ Cathode Material. In Proceedings of the International Conference on Materials Research and Innovation (ICMARI 2021), Bangkok, Thailand, 15–17 December 2021; Volume 1234, p. 012029. https://doi.org/10.1088/1757-899x/1234/1/012029.
13. Li, X.; Zhou, Q.; Zhang, X.; et al. High Electrochemical Performance Recycling Spent LiFePO4 Materials through the Preoxidation Regeneration Strategy. *ACS Sustain. Chem. Eng.* **2023**, *11*, 14457–14466. https://doi.org/10.1021/acssuschemeng.3c03232.
14. He, J. Classification and Application Research of Lithium Electronic Batteries. In Proceedings of the 2023 International Conference on Materials Engineering, New Energy and Chemistry (MENEC 2023), Kuala Lumpur, Malaysia, 13–15 October 2023; p. 03008. https://doi.org/10.1051/matecconf/202338603008.
15. Yue, Y.; Li, S.; Cheng, X.; et al. Effects of Temperature on the Ohmic Internal Resistance and Energy Loss of Lithium-Ion Batteries under Millisecond Pulse Discharge. In Proceedings of the 2022 International Conference on Advanced Electronics, Electrical and Green Energy (AEEGE 2022), Chongqing, China, 19–22 May 2022. https://doi.org/10.1088/1742-6596/2301/1/012014.
16. Yue, P. Introduction of LFP and Ternary Cathode Materials of Lithium Battery. *Highlights Sci. Eng. Technol.* **2023**, *58*, 387–394. https://doi.org/10.54097/hset.v58i.10127.
17. Fan, T.; Liang, W.; Guo, W.; et al. Life cycle assessment of electric vehicles' lithium-ion batteries reused for energy storage. *J. Energy Storage* **2023**, *71*, 108126. https://doi.org/10.1016/j.est.2023.108126.
18. Zhao, T.; Li, W.; Traversy, M.; et al. A review on the recycling of spent lithium iron phosphate batteries. *J. Environ. Manag.* **2024**, *351*, 119670. https://doi.org/10.1016/j.jenvman.2023.119670.
19. Liu, Y.; Zhang, C.; Hao, Z.; et al. Study on the Life Cycle Assessment of Automotive Power Batteries Considering Multi-Cycle Utilization. *Energies* **2023**, *16*, 6859. https://doi.org/10.3390/en16196859.
20. Hu, H.; Yang, G.; Chen, C.; et al. Ultra-Selective and Capacious Lithium Extraction from Geothermal Brines via β−Diketone Functionalized Brush-Shaped Polymer. *Adv. Funct. Mater.* **2025**, *35*, e13012. https://doi.org/10.1002/adfm.202513012.
21. Liu, G.; Chen, Z.; Liu, T.; et al. Interlayer Dual-Sieving Engineering of Al-Intercalated MoS_2 for Ultrafast and Selective Lithium Recovery from High-Sodium Lithium-Bearing Brine. *Adv. Mater.* **2026**, *38*, e73654. https://doi.org/10.1002/adma.73654.
22. Jiang, Z.; Zhu, P.; Yang, Y.; et al. Sustainable recovery of lithium from spent $LiFePO_4$ via proton circulation. *Chem. Eng. J.* **2023**, *466*, 143186. https://doi.org/10.1016/j.cej.2023.143186.
23. Feng, Y.; Xie, Y.; Yang, L.; et al. Precise recovery of highly-purified iron phosphate from complex lithium extraction slag leach solution: Theory guiding experiment. *Sep. Purif. Technol.* **2024**, *347*, 127605. https://doi.org/10.1016/j.seppur.2024.127605.
24. Gao, M.; Sun, F.; Peng, W.; et al. Green and efficient method for the realization of full-component recovery of $LiFePO_4$ black powder. *Green Chem.* **2024**, *26*, 7377–7383. https://doi.org/10.1039/d4gc01444h.
25. Jing, C.; Tran, T.T.; Lee, M.S. A Review on the Recovery of Lithium and Iron from Spent Lithium Iron Phosphate Batteries. *Miner. Process. Extr. Metall. Rev.* **2024**, *45*, 892–903. https://doi.org/10.1080/08827508.2024.2305382.
26. Jing, Q.; Zhang, J.; Liu, Y.; et al. Direct Regeneration of Spent $LiFePO_4$ Cathode Material by a Green and Efficient One-Step Hydrothermal Method. *ACS Sustain. Chem. Eng.* **2020**, *8*, 17622–17628. https://doi.org/10.1021/acssuschemeng.0c07166.
27. Li, Z.; Liu, D.; Xiong, J.; et al. Selective recovery of lithium and iron phosphate/carbon from spent lithium iron phosphate cathode material by anionic membrane slurry electrolysis. *Waste Manag.* **2020**, *107*, 1–8. https://doi.org/10.1016/j.wasman.2020.03.017.
28. Yadav, P.; Jie, C.J.; Tan, S.; et al. Recycling of cathode from spent lithium iron phosphate batteries. *J. Hazard. Mater.* **2020**, *399*, 123068. https://doi.org/10.1016/j.jhazmat.2020.123068.
29. Song, X.; Cao, Y.; Zhang, Y.; et al. Preparation and characterization of nanoscale flaky iron phosphate from phosphating slag. In Proceedings of the IOP Conference Series: Materials Science and Engineering, 6th Annual International Conference on Material Science and Engineering (ICMSE2018), Suzhou, China, 22–24 June 2018; Volume 397, p. 012001. https://doi.org/10.1088/1757-899x/397/1/012001.
30. Tu, T.; Yu, X.; Liu, Q. Efficient recovery of phosphorus and iron from the lithium extraction slag by the leaching precipitation method. *Can. Metall. Q.* **2025**, *64*, 644–652. https://doi.org/10.1080/00084433.2024.2357856.
31. Huang, L.; Zhang, C.-Z.; Tan, J.; et al. Recycling $FePO_4 \cdot 2H_2O$ from waste $LiFePO_4$ powders and formation mechanisms of the impurities during precipitation process. *Chin. J. Inorg. Chem.* **2023**, *39*, 357–366.

32. Bian, D.; Sun, Y.; Li, S.; et al. A novel process to recycle spent $LiFePO_4$ for synthesizing $LiFePO_4$/C hierarchical microflowers. *Electrochim. Acta* **2016**, *190*, 134–140. https://doi.org/10.1016/j.electacta.2015.12.114.
33. Asakai, T.; Hioki, A. Comparison of three electrochemical end-point detection methods to assay potassium dichromate by coulometric titration. *Accredit. Qual. Assur.* **2012**, *17*, 45–52. https://doi.org/10.1007/s00769-011-0834-6.
34. Kadowaki, Y.; Yanagihara, Y.; Inagawa, A.; et al. Quantitative Reduction of Iron under Nitrogen Atmosphere for Potassium Dichromate Titration. *ISIJ Int.* **2024**, *64*, 1416–1426. https://doi.org/10.2355/isijinternational.isijint-2024-066.
35. Hu, H.; Tang, Y.; Ying, H.; et al. The effect of copper on iron reduction and its application to the determination of total iron content in iron and copper ores by potassium dichromate titration. *Talanta* **2014**, *125*, 425–431. https://doi.org/10.1016/j.talanta.2014.03.008.
36. Qiu, X.; Zhang, B.; Xu, Y.; et al. Enabling the sustainable recycling of $LiFePO_4$ from spent lithium-ion batteries. *Green Chem.* **2022**, *24*, 2506–2515. https://doi.org/10.1039/d1gc04784a.
37. Chang, X.; Fan, M.; Gu, C.F.; et al. Selective Extraction of Transition Metals from Spent $LiNi_xCo_yMn_{1-x-y}O_2$ Cathode via Regulation of Coordination Environment. *Angew. Chem. Int. Ed.* **2022**, *61*, e202202558. https://doi.org/10.1002/anie.202202558.
38. Zhang, Y.; Wang, B.; Wang, F.; et al. A green recyclable process for selective recovery of Li and Fe from spent lithium iron phosphate batteries by synergistic effect of deep eutectic solvent and oxygen. *Sep. Purif. Technol.* **2025**, *354*, 128764. https://doi.org/10.1016/j.seppur.2024.128764.
39. Fan, E.; Li, L.; Zhang, X.; et al. Selective Recovery of Li and Fe from Spent Lithium-Ion Batteries by an Environmentally Friendly Mechanochemical Approach. *ACS Sustain. Chem. Eng.* **2018**, *6*, 11029–11035. https://doi.org/10.1021/acssuschemeng.8b02503.
40. Zhang, L.; Brow, R.K. A Raman Study of Iron–Phosphate Crystalline Compounds and Glasses. *J. Am. Ceram. Soc.* **2011**, *94*, 3123–3130. https://doi.org/10.1111/j.1551-2916.2011.04486.x.
41. Frost, R.L.; Xi, Y.; Scholz, R.; et al. Infrared and Raman spectroscopic characterization of the phosphate mineral kosnarite $KZr_2(PO_4)_3$ in comparison with other pegmatitic phosphates. *Transit. Met. Chem.* **2012**, *37*, 777–782. https://doi.org/10.1007/s11243-012-9652-x.